

Structure of catalytically active Rh–In bimetallic phase for amination of alcohols†

Cite this: *RSC Adv.*, 2014, 4, 28664

Tsukasa Takanashi, Masazumi Tamura, Yoshinao Nakagawa* and Keiichi Tomishige*

The structure of Rh–In bimetallic catalysts supported on carbon for amination of alcohols was determined by XRD, TEM-EDX, XPS, CO adsorption and EXAFS. At low In/Rh ratio ($\text{In/Rh} \leq 0.2$), Rh metal particles with sizes of <3 nm were observed, and the particles were partially covered with indium oxide species. With addition of more In, a tetragonal RhIn alloy with a particle size of ~ 20 nm was formed. This tetragonal alloy has a structure with $a = 0.315$ nm and $c = 0.328$ nm where metal atoms are located at (0, 0, 0) and (0.5, 0.5, 0.5). The catalytic activity of the tetragonal RhIn alloy is much higher than that of Rh metal particles with or without indium oxide species. With an excess amount of In ($\text{In/Rh} > 1$) on the high Rh loading (20 wt%) catalyst, the cubic RhIn phase with a CsCl structure was observed instead of the tetragonal RhIn phase, and the catalytic activity was much decreased.

Received 1st May 2014
Accepted 17th June 2014

DOI: 10.1039/c4ra03984j

www.rsc.org/advances

1. Introduction

Supported bimetallic catalysts can sometimes promote reactions that do not proceed over monometallic catalysts, and are an important class of heterogeneous catalysts.^{1–3} The structure of bimetallic particles generally much affects the catalytic performance, and therefore characterization of the catalysts is essential. We have very recently discovered that Rh–In supported on carbon can catalyze the amination of alcohols in ammonia water, while monometallic Rh/C and In/C are almost inactive.⁴ Amination of alcohols (eqn (1)) is one method of amine production, and the advantages over conventional amine production methods such as reductive amination of carbonyl compounds include inexpensive starting material and high atom efficiency.^{5–7}



Some Rh-based bimetallic catalysts such as those using Sn, Mo, and Re have been reported to show unique activity and/or selectivity in reductive transformations of organic molecules, and the structures have been intensively investigated.^{8–17} On the other hand, the combination of noble metal and In has been rarely studied for catalyst materials^{18,19} except Pt–In system.^{20–24} Even for bulk material, the structure or use of Rh–In alloy system has not been so intensively studied.^{25,26} The known phases of Rh–In alloy are RhIn with cubic CsCl structure ($a = 0.320$ nm) and RhIn₃ with tetragonal CoGa₃ structure ($a = 0.701$ nm, $c = 0.715$ nm).²⁷ The existence of Rh-rich Rh–In phase

has been suggested; however not identified.²⁸ In the previous paper, we characterized Rh–In/C catalyst with 5 wt% Rh and In/Rh = 1 with XRD, TEM and XPS.⁴ The data suggested the formation of RhIn alloy; however, because of the small loading amount and broad XRD signals it is difficult to determine the structure of catalytically active species. In this study, we investigated the structure of carbon-supported Rh–In catalysts with large Rh loadings and different In/Rh ratio in order to clarify the relationship between the structure and catalytic activity. We found a catalytically active RhIn phase with tetragonal structure that has not been reported in the literature.

2. Experimental section

2.1. Catalyst preparation

Rh/C and In/C catalysts were prepared by impregnating the carbon (Shirasagi FAC-10, BET surface area 851 m² g^{−1}; Japan EnviroChemicals, Ltd.) with an aqueous solution of RhCl₃·3H₂O (Soekawa Chemical Co., Ltd.) and In(NO₃)₃·3H₂O (Wako Pure Chemical Industries, Ltd.), respectively. The Rh–In/C catalysts were prepared by a co-impregnation method using the carbon support and mixed aqueous solution of RhCl₃·3H₂O and In(NO₃)₃·3H₂O. The loading amount of Rh was 5 or 20 wt%, and that of In was 0.1–2 by molar ratio of In to Rh. After impregnation, the catalysts were dried at 383 K for half a day and reduced under H₂ flowing at 773 K for 3 h. For Rh 5 wt% catalysts, they were heated under N₂ flowing at 773 K for 3 h after drying followed by reduction under H₂ flowing at 773 K for 3 h, as reported in the previous paper.⁴

2.2. Characterization of the catalysts

The concentration of indium in the catalysts was determined by X-ray fluorescence spectroscopy (XRF) using a Bruker AXS K.K.,

Department of Applied Chemistry, School of Engineering, Tohoku University, 6-6-07, Aoba, Aramaki, Aoba-ku, Sendai 980-8579, Japan. E-mail: tomi@erec.che.tohoku.ac.jp; yoshinao@erec.che.tohoku.ac.jp; Fax: +81-22-795-7214; Tel: +81-22-795-7214

† Electronic supplementary information (ESI) available. See DOI: 10.1039/c4ra03984j

S8 Tiger spectrometer with the wavelength dispersive system. The pretreated catalyst powders were mixed with cellulose and Sn as binder and internal standard, respectively, and then compressed to 10 ϕ pellets with about 2 mm thickness. The weight concentration of indium was determined by calibration curve method.

The XRD patterns of the reduced catalysts were recorded on a Rigaku MiniFlex600 diffraction-meter using Cu K α ($\lambda = 0.154$ nm) generated at 40 kV and 15 mA. The catalysts with various In/Rh molar ratios were reduced under H₂ flowing at 773 K for 3 h. The reduced catalyst powders were transferred to the sample holder filled with N₂ without exposing air in the glove bag. The average particle size of metal was estimated using the Scherrer equation. Dispersion of Rh particles (the ratio of surface atoms to total atoms; Rh_s/Rh) was calculated by the equation: Rh_s/Rh = 1.098 nm/(particle size).²⁹ XRD pattern of model structure was calculated with CrystalDiffract for Windows ver. 1.4 software (CrystalMaker Software Ltd.).

The amount of CO chemisorption was measured in a high-vacuum system using a volumetric method. Before adsorption measurements, the catalysts were treated with H₂ at 773 K for 3 h. Subsequently, the adsorption was performed at room temperature. The gas pressure at adsorption equilibrium was about 1.1 kPa. The sample weight was about 0.15 g. The dead volume of the apparatus was about 80 cm³. The adsorption amount of CO is represented as the molar ratio to Rh.

The X-ray photoelectron spectra (XPS) were recorded using a Shimadzu AXIS-ULTRA with monochromatic Al K α irradiation ($h\nu = 1486.6$ eV). The spot size of the X-ray was ca. 700 \times 300 μm^2 . The catalysts were reduced in flowing H₂ at 773 K for 3 h, and then, the reduced catalysts were transported to the analysis chamber in N₂ atmosphere. The spectra were analyzed with the program CasaXPS software, version 2.3.16. A binding energy of 284.5 eV of the C 1s level was used as an internal standard. The curve fitting of the In 3d level spectra was conducted with Voigt lineshapes and a Shirley background function.

Field emission-scanning transmission electron microscope (FE-STEM) images and EDX analysis were obtained on a Hitachi spherical aberration corrected STEM/SEM HD-2700 instrument operated at 200 kV. The reduced catalyst was dispersed in ethanol in the glove bag. Then dispersed sample was deposited on a Cu grid in air. The measurement was begun within 10 minutes after deposition.

The X-ray absorption fine structure (XAFS) spectra were measured at the BL01B1 station at SPring-8 with the approval of the Japan Synchrotron Radiation Research Institute (JASRI; proposal no. 2013B1067). The storage ring was operated at 8 GeV. A Si (1 1 1) single crystal was used to obtain a monochromatic X-ray beam. Two ion chambers for I_0 and I were filled with Ar for Rh and In K-edge measurement. We measured the XAFS spectra of the catalysts after reduction with flowing H₂ at 773 K for 3 h. The reduced catalyst powders were transferred to the measurement cell without exposing air in the glove bag. The thickness of the cell filled with the powder was 1 cm to give an edge jump of 0.8–4.0 and 0.1–1.0 for Rh K-edge and In K-edge measurement, respectively. The XAFS data were collected in a

transmission mode. For extended XAFS (EXAFS) analysis, the oscillation was first extracted from the EXAFS data using a spline smoothing method. Oscillation was normalized by the edge height around 50 eV. Fourier transformation of the k^3 -weighted EXAFS oscillation from the k space to the r space was performed to obtain a radial distribution function. The inversely Fourier filtered data were analyzed using a usual curve fitting method. For curve fitting analysis, the empirical phase shift and amplitude functions for the In–O bonds and metallic bonds such as Rh–Rh, In–In, Rh–In and In–Rh were extracted from data for Rh₂O₃ and Rh foil, respectively, because of the similar behavior of Rh and In as backscattering atoms in EXAFS and the complex structures of In metal and In₂O₃. Analyses of XAFS data were performed using a computer program (REX2000, ver. 2.5.9; Rigaku Corp.) for both EXAFS and XANES (X-ray adsorption near edge structure).

2.3. Procedure for the activity test in the amination of alcohol

Activity tests of 1,2-propanediol (Wako Pure Chemical Industries, Ltd.) were performed in a 190 ml autoclave with an inserted glass vessel. Substrate (10 mmol), aqueous ammonia supplied by Wako Pure Chemical Industries, Ltd. (28 wt%, 0.1 mol), catalyst (50 mg), a spinner and water were placed into the autoclave. The total volume of the reaction solution was adjusted to 20 ml by addition of water. After sealing the reactor, the N₂ content was purged by flushing three times with 1 MPa H₂. The reactor was filled with 5 MPa H₂ at room temperature and then heated to the reaction temperature (453 K). The temperature was monitored using a thermocouple inserted in the reactor. During the experiment, the stirring rate was fixed at 500 rpm. After 24 h, the reactor was cooled down and the gases were collected in a gas bag. The reactor contents were transferred to a vial, and the catalyst was separated by filtration. Then reaction solution was diluted by water to analysis. The products in both liquid and gas phases were analyzed by a gas chromatograph (Shimadzu GC-2014) equipped with InertCap for amines column (GL Sciences Inc.). The selectivity was calculated in carbon basis.

3. Results and discussion

3.1. Sample preparation and loading amount

We prepared Rh–In/C catalysts with 20 wt% Rh loading amount, in addition to those with 5 wt% Rh as reported in the previous study,⁴ in order to characterize the bimetallic phase more clearly. We applied co-impregnation method to the catalyst preparation, and the method could bring all the used precursors on to the support. However, after calcination and reduction of the sample with larger Rh and In loadings, some amount of yellow–orange solid was deposited at the end of reactor tube. The solid was probably In₂O₃ considering the low melting point of In metal (430 K).³⁰ We therefore analyzed the actual loading amount of In on the reduced sample with XRF. The XRF data are shown in Table 1. Although significant loss of In was observed for the sample with very large In loading (In/Rh = 2, nominally),

Table 1 XRF analysis of Rh–In/C (Rh 20 wt%)

In/Rh in preparation	In/Rh from XRF	In loss/%
1.0	1.0	2
1.5	1.4	7
2.0	1.6	18

the loss of In from the sample with smaller In loading (In/Rh = 1) was negligible. We use the nominal value of In/Rh ratio of the samples in the following sections.

3.2. Catalytic performance of Rh–In/C (20 wt%) with different In loading amount, and the difference between Rh 20 wt% and 5 wt% catalysts

The results of activity tests of Rh–In/C (Rh 20 wt%) for 1,2-propanediol amination are shown in Fig. 1. The products were 2-amino-1-propanol, 1-amino-2-propanol, and the dimerization products (2,5- and 2,6-dimethylpiperazines) (Scheme 1). The catalyst without In (Rh/C) showed very low activity. The substrate conversion as a function of In amount showed a volcano curve, and the catalyst with In/Rh = 0.5 gave the highest conversion. The selectivity to aminopropanols was increased with increasing In amount. The ratio of 1-amino-2-propanol/2-amino-1-propanol was almost 1 and was independent of In/Rh

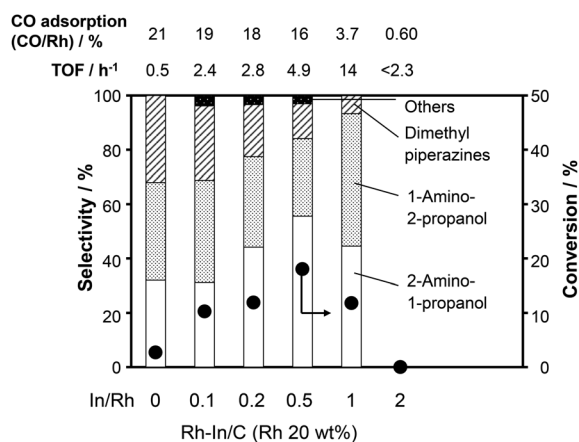
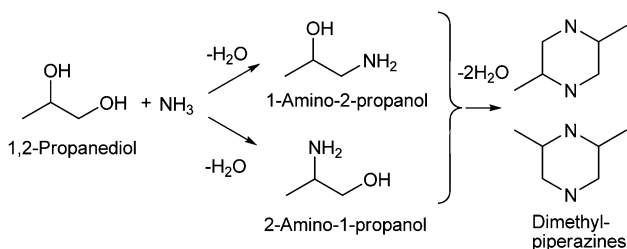


Fig. 1 Catalytic performance of Rh–In/C (Rh 20 wt%) for amination of 1,2-propanediol. Reaction conditions: water 13.2 g, 1,2-propanediol 0.76 g, NH₃aq 6.08 g (total 20 ml), catalyst 50 mg, H₂ 5 MPa (at r.t.), 453 K, 24 h.



Scheme 1 Amination of 1,2-propanediol.

ratio. We calculated the turnover frequency (TOF) as defined in eqn (2) to assess the catalytic activity, and the values are also listed in Fig. 1.

$$\text{TOF (h}^{-1}\text{)} = \frac{\text{(converted substrate (mol))}}{\{\text{(amount of CO adsorption (mol))} \times \text{(reaction time (h))}\}} \quad (2)$$

The amount of CO adsorption corresponds the amount of surface metallic Rh atoms, since In metal or metal oxides do not adsorb CO. The CO adsorption amount was gradually decreased from In/Rh = 0 to 0.5 and was rapidly decreased by further addition of In. The TOF value was much increased with increasing In amount from In/Rh = 0.2 to 1, and the catalyst with In/Rh = 1 showed the highest TOF value (14 h⁻¹). However, further addition of In much decreased the catalytic activity: when In/Rh = 2, the catalyst showed no activity (TOF < 2.3 h⁻¹). The catalytic performances of Rh–In/C catalysts with smaller Rh amount (5 wt%) in the same reaction conditions as those in Fig. 1 have been reported in the previous paper.⁴ Both series of catalysts (Rh 20 wt% and 5 wt%) have similar trends of performance when In/Rh ratio is 1 or less: the activity of Rh/C without In is very low; the catalysts with low In/Rh have low activity; the TOF value is much increased by In addition from In/Rh = 0.2 to 1; the selectivity to amino alcohols is increased with increasing In/Rh, and the ratio of 1-amino-2-propanol/2-amino-1-propanol is almost constant. It should be noted that both series of catalysts with Rh 20 wt% and 5 wt% showed similar TOF values for low In/Rh ratio (In/Rh = 0.1 and 0.2; TOF ~3 h⁻¹) and similar highest TOF values (14 and 15 h⁻¹ for Rh 20 wt% and 5 wt%, respectively). The highest TOF values were obtained when In/Rh = 1 for both series. However, when In/Rh = 2, the catalysts with different Rh loadings showed different behavior: the catalyst with Rh 20 wt% (Fig. 1) showed almost no activity, while the catalyst with Rh 5 wt% has moderate activity (TOF 10 h⁻¹). Overall, these data suggest that the structures of supported phases are similar for both series of catalysts (Rh 20 wt% and 5 wt%) when In/Rh = 1 or less.

3.3. Characterization of Rh–In/C: XRD

Fig. 2 shows the XRD patterns of reduced Rh–In/C (Rh 20 wt%) catalysts under inert atmosphere. The patterns can be classified into three groups based on In/Rh ratio: (i) In/Rh ≤ 0.2, (ii) 0.2 < In/Rh ≤ 1, and (iii) In/Rh > 1. The pattern of group (i) had the peaks of fcc Rh. The pattern of group (iii) had the intense peaks of cubic RhIn (PDF 59516). The pattern of group (ii) showed the peaks different from those of fcc Rh and cubic RhIn. The pattern was composed of pairs of peaks with intensity ratio of 2 : 1. The peak positions were almost unaffected by the difference of In/Rh ratio and were similar to those of cubic RhIn. Each pair corresponded to a peak of cubic RhIn. We conducted fitting of the calculated peak patterns to the pattern of group (ii) by distortion of cubic RhIn structure. The distortion along the z-axis well fitted the peak split, and the tetragonal structure with *a* = 0.315 nm and *c* = 0.328 nm gave the best fit (Fig. 3). However, since the atomic number of Rh and In is similar, the distribution of Rh/In atoms cannot be determined based on the

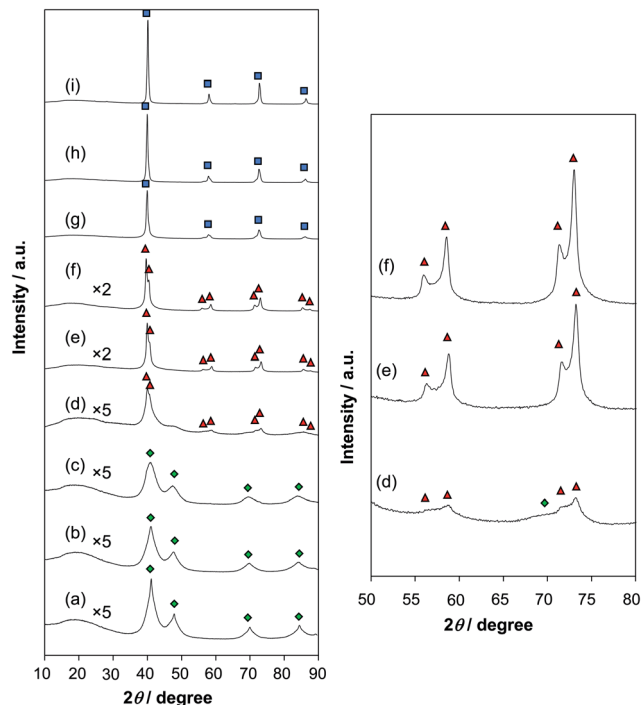


Fig. 2 XRD patterns of Rh–In/C (Rh 20 wt%) with different indium amount. (a) Rh/C, (b–i) Rh–In/C; (b) In/Rh = 0.1, (c) In/Rh = 0.2, (d) In/Rh = 0.5, (e) In/Rh = 0.75, (f) In/Rh = 1, (g) In/Rh = 1.2, (h) In/Rh = 1.5, (i) In/Rh = 2. \blacklozenge : fcc Rh metal, \blacktriangle : tetragonal alloy, \blacksquare : cubic RhIn.

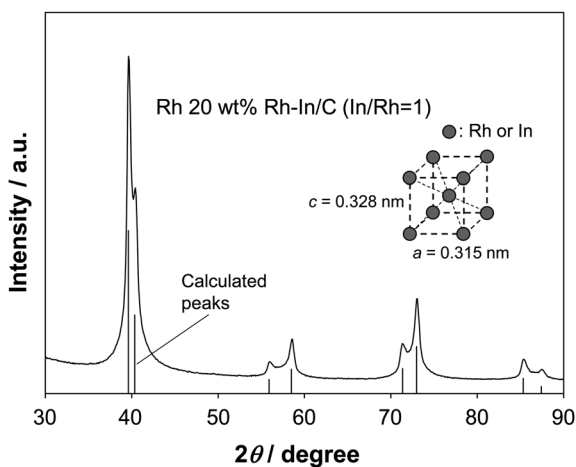


Fig. 3 Calculated and observed XRD patterns of Rh–In/C (In/Rh = 1).

XRD patterns at this stage; the distributions will be discussed in Section 3.5. The XRD patterns of Rh–In/C (Rh 5 wt%) are shown in Fig. S1 (ESI),[†] where similar structure change is evident from fcc Rh phase to alloy phase with CsCl (or CsCl-like) structure between In/Rh = 0.2 and 0.5. However, the XRD peaks in In/Rh \geq 0.5 samples were too broad to distinguish tetragonal (group (ii)) and cubic (group (iii)) phases.

The XRD of Rh–In/C (Rh 20 wt%, In/Rh = 1) after reaction was also measured, and the pattern was almost unchanged from that of the fresh reduced sample (Fig. S2, ESI[†]). The reusability of Rh–In/C catalyst has been confirmed in the

previous paper.⁴ Therefore, the structure of reduced catalyst surely reflects the catalytic performance.

Comparison with the results of activity tests (Fig. 1) shows that the catalytic activity is in the following order: group (ii) > group (i) \gg group (iii) \sim 0. The very low activity of group (iii) (Rh–In/C (Rh 20 wt%, In/Rh > 1)) indicates that the cubic RhIn species is not catalytically active. The high activity of group (ii) suggests the activity of tetragonal alloy phase; however this idea has not been fully proven because another active phase may exist which does not appear in XRD (amorphous or very small size). We further characterized each group of catalysts.

3.4. Characterization of Rh–In/C (Rh 20 wt%, In/Rh \leq 0.2) (group (i))

The XRD peak positions (Fig. 2) were not changed by different In amount, indicating that alloy was not formed. Table 2 shows the Rh particle size determined by the width of XRD peak. The CO adsorption amount is also shown in Table 2. The particle size was decreased with increasing In amount, which means that more atoms in the particles are located on the surface. On the other hand, the CO adsorption amount, which means the amount of surface Rh atoms, was slightly decreased with increasing In amount. This type of discrepancy has been frequently observed for supported bimetallic catalysts that consist of noble metal + non-noble metal,^{9,10,31–33} and it can be explained by the partial covering of noble metal particle (Rh) with non-noble metal (In) species. We further pay attention to the difference between surface Rh atoms calculated by XRD and those determined by CO adsorption (Rh_s/Rh – CO/Rh). The (Rh_s/Rh – CO/Rh) value was increased by In addition, and the increase was almost the same as the amount of In addition. This agreement suggested that all added In atoms interacted with Rh surface assuming that covering with one In atom blocks one adsorption site.

The In 3d XPS data are shown in Fig. 4. Each peak can be fitted by one single function, and all the peak positions (444.5 and 444.6 eV for 3d_{5/2}; 452.0 and 452.1 eV for 3d_{3/2}) are within the range for In(III) species (3d_{5/2}: 444.26–444.84 eV, 3d_{3/2}: 451.80–452.38 eV).³⁴ The absence of In(0) signal supported the absence of Rh–In alloy. The summary of XPS data for all samples is shown in ESI (Table S1).[†]

Based on the data, we propose the model structure of this group of catalyst (Fig. 5). The Rh metal particles are formed on the carbon support, and all the added In atoms are located on the Rh particle surface as In(III) oxide. The comparison between the structure (Fig. 5) and catalytic activity (Fig. 1) shows that the modification of Rh metal with indium oxide generates the catalytic activity in the amination.

Table 2 Rh particle size of Rh–In/C (Rh 20 wt%; In/Rh \leq 0.2)

In/Rh	Particle size/nm from XRD	Rh _s /Rh from XRD	CO/Rh	Rh _s /Rh – CO/Rh
0	3.7	0.30	0.21	0.09
0.1	2.8	0.39	0.19	0.20
0.2	2.3	0.48	0.18	0.30

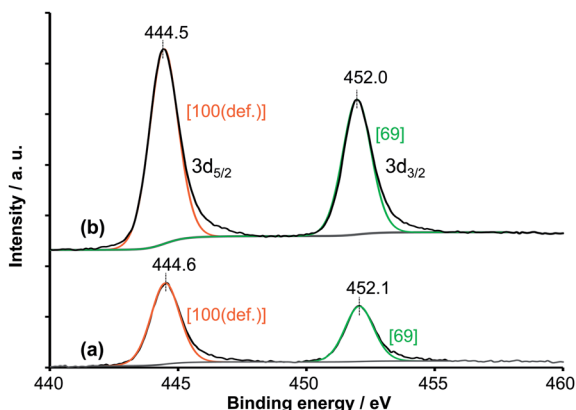


Fig. 4 In 3d XPS of Rh–In/C (Rh 20 wt%, In/Rh = 0.1 (a) and 0.2 (b)). []: area ratio.

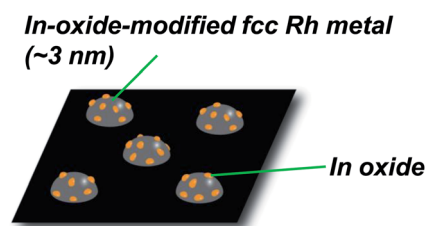


Fig. 5 Structure model of Rh–In/C (Rh 20 wt%, In/Rh \leq 0.2).

The state of Rh and In was also investigated with EXAFS. The results of Fourier transform and curve fitting are shown in Fig. 6 and Table 3, respectively. The EXAFS oscillation and Fourier filtered EXAFS data are shown in ESI (Fig. S3 and S4).[†] The Rh K-edge EXAFS data were well fitted by single Rh–Rh shell with coordination number (CN) \sim 11, supporting that all Rh atoms were in the metallic state. The In K-edge EXAFS data can be fitted by In–O shell and In–Rh shell as expected by the model structure as shown in Fig. 5.

3.5. Characterization of Rh–In/C (Rh 20 wt%, 0.2 < In/Rh \leq 1) (group (ii))

The XRD data (Fig. 2) showed that the main species of this group was tetragonal Rh–In alloy. When the In amount was

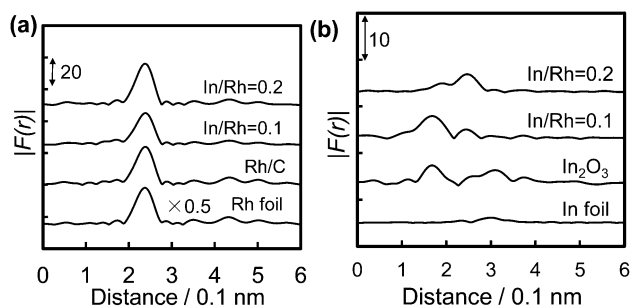


Fig. 6 Results of Fourier transform of k^3 -weighted EXAFS oscillation of Rh–In/C (Rh 20 wt%, In/Rh \leq 0.2). (a) Rh K-edge, FT range: 30–150 nm^{-1} ; (b) In K-edge, FT range: 30–120 nm^{-1} .

smaller, the phase of fcc Rh metal was also evident. These pattern changes and the characterization results in the above section suggest that the addition of In above In/Rh = 0.2 causes the phase change from indium-oxide-modified Rh metal particles into tetragonal Rh–In alloy. The In 3d XPS data of Rh–In/C (Rh 20 wt%, In/Rh = 0.5, 1) are shown in Fig. 7. Each peak can be fitted by two functions. The peak positions of the functions with higher binding energy were within the range of In(III), and those at lower binding energy were almost the same as In metal (443.9 and 451.4 eV (ref. 34)). Therefore the samples contained both In(0) and In(III) species. The ratio of In(0) to (In(0) + In(III)) within the effective escape depth was determined to be 50% and 65% for the sample of In/Rh = 0.5 and 1, respectively. The increasing amount of In(0) supports the formation of Rh–In alloy.

The TEM images and EDX analyses of Rh–In/C (Rh 20 wt%, In/Rh = 1) are shown in Fig. 8 and 9, respectively. Surprisingly, large dendritic structure was present as well as carbon-supported particles. The dendritic structure was composed of domains with the size of 10–30 nm. The particles on the support had various sizes from <5 nm to \sim 20 nm. The EDX analysis was conducted with either Cliff–Lorimer method,³⁵ which gives the average element ratio in the total field of image, or conventional line analysis. The results showed that both dendritic structure and carbon-supported particles had the In/Rh ratio of 1.0. We also measured the mapping of elemental distributions (Fig. S5, ESI[†]), which also confirmed the bimetallic structure. From XRD, the particle size of tetragonal Rh–In alloy in Rh–In/C (Rh 20 wt%, In/Rh = 1) was calculated to be 20 nm. In this calculation, we assumed that the broadening by the heterogeneity of alloy composition did not affect the peak width since the change of In/Rh ratio did not affect the XRD peak positions. Based on TEM-EDX and XRD, we determined the phase of both the dendritic structure and the larger particles on the support as tetragonal RhIn alloy with the atomic ratio of 1 : 1. The analogy with cubic RhIn alloy with CsCl structure suggests that the Rh and In atoms in tetragonal RhIn alloy are located at (0, 0, 0) and (0.5, 0.5, 0.5), respectively, in the unit cell as similar to CsCl structure. It is not known why tetragonal RhIn alloy was formed on this catalyst rather than well-known cubic RhIn alloy. One factor may be the shortage of In. In the literature, cubic RhIn phase has been reported to exist in slightly indium-rich conditions of In + Rh system: from In/(In + Rh) = 51% to 56% at 873 K.²⁸

Fig. 10 and Table 4 show the Fourier transform and the curve fitting results of EXAFS, respectively. The EXAFS oscillation and Fourier filtered EXAFS data are shown in ESI (Fig. S3 and S4).[†] The Rh K-edge EXAFS data can be fitted by three Rh–Rh (or In) shells, which consists of one shell for fcc Rh structure ($R = 0.268$ nm) and two shells for bcc-like structure ($R = 0.28$ and 0.32 nm; ratio of CN = 8/6). The latter shells corresponded to the tetragonal RhIn alloy. The CN of Rh–Rh shell for fcc Rh structure was decreased and the CNs for RhIn alloy were increased with increasing In amount. This behavior supports the transformation of fcc Rh particles, probably modified with indium species, into RhIn alloy by addition of indium. The In(III) species detected by XPS analysis (Fig. 7) can be assigned to the In species covering the fcc Rh metal particles. The In K-edge

Table 3 EXAFS curve fitting results of Rh–In/C (Rh 20 wt%; In/Rh \leq 0.2)

Sample (In/Rh)	Edge	Shell	CN ^a	R ^b nm	σ^c /nm	ΔE_0^d /eV	R _f ^e /%	Fourier filtering range/nm
0	Rh K	Rh–Rh	11.1	0.268	0.0079	3.0	0.6	0.166–0.292
0.1	Rh K	Rh–Rh (or –In)	10.8	0.268	0.0084	5.3	1.2	0.166–0.292
		In–O	2.1	0.211	0.0060	–9.6	2.4	
	In K	In–O	2.4	0.225	0.0060	–0.3		
		In–Rh (or –In)	1.2	0.271	0.0083	5.5		
0.2	Rh K	Rh–Rh (or –In)	10.5	0.268	0.0077	3.4	1.0	0.166–0.292
		In–O	1.4	0.211	0.0076	2.4	2.2	
	In K	In–O	1.6	0.225	0.0078	–4.6		
		In–Rh (or –In)	2.3	0.271	0.0083	0.4		
Rh foil	Rh K	Rh–Rh	12	0.268	0.0060	0	—	—
Rh ₂ O ₃	Rh K	Rh–O	6	0.206	0.0060	0	—	—

^a Coordination number. ^b Bond distance. ^c Debye–Waller factor. ^d Difference in the origin of photoelectron energy between the reference and the sample. ^e Residual factor.

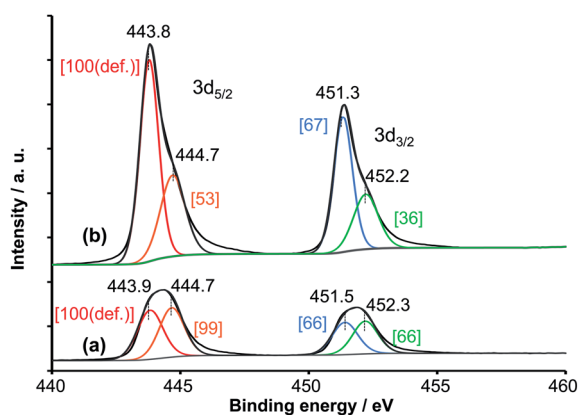


Fig. 7 In 3d XPS of Rh–In/C (Rh 20 wt%, In/Rh = 0.5 (a) and 1 (b)). []: area ratio.

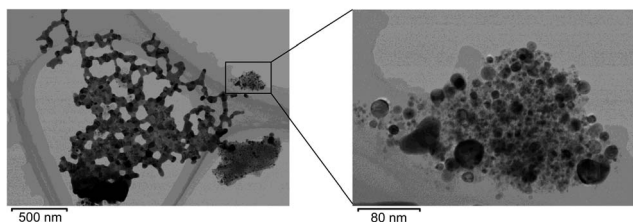


Fig. 8 TEM images of Rh–In/C (Rh 20 wt%, In/Rh = 1).

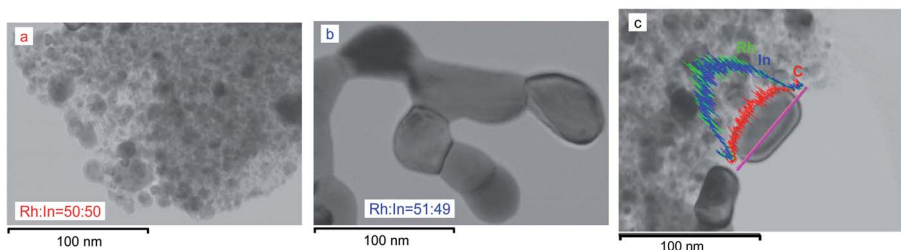


Fig. 9 TEM-EDX analysis of Rh–In/C (Rh 20 wt%, In/Rh = 1). (a) and (b): Cliff–Lorimer method for the elemental analysis in the whole area. (c) Line analysis.

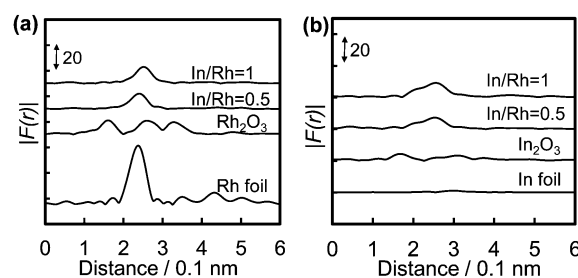


Fig. 10 Results of Fourier transform of k^3 -weighted EXAFS oscillation of Rh–In/C (Rh 20 wt%, In/Rh = 0.5 and 1). (a) Rh K-edge, FT range: 30–150 nm⁻¹; (b) In K-edge, FT range: 30–120 nm⁻¹.

EXAFS data can be fitted by two In–metal (metal = Rh or In) shells and In–O shell. The two In–metal shells had almost the same distances (R) as those of Rh–metal shells for the bcc-like structure. In addition, the number of In–metal bond calculated by (CN of In–metal shell) \times (number of In atoms in the sample) was almost the same as the number of Rh–metal bond (= (CN of Rh–metal shell) \times (number of Rh atoms in the sample)) with similar distance. These similarities further support the formation of bcc-like RhIn alloy where Rh and In are structurally equal.

The molar ratio of tetragonal RhIn alloy to total Rh can be calculated from the ratio of the CN of the shells of bcc-like tetragonal phase to the theoretical values (8 and 6 for $R = 0.28$

Table 4 EXAFS curve fitting results of Rh–In/C (Rh 20 wt%; In/Rh = 0.5 and 1)

Sample (In/Rh)	Edge	Shell	CN ^a	R ^b nm	σ ^c /nm	ΔE ₀ ^d /eV	R _f ^e /%	Fourier filtering range/nm
0.5	Rh K	Rh–Rh (or –In)	6.0	0.268	0.0076	6.6	1.0	0.166–0.292
		Rh–Rh (or –In)	2.8	0.277	0.0068	3.4		
		Rh–Rh (or –In)	2.2	0.320	0.0088	8.8		
	In K	In–O	0.7	0.223	0.0073	9.9	2.2	0.126–0.279
		In–Rh (or –In)	5.4	0.277	0.0077	6.4		
		In–Rh (or –In)	4.0	0.319	0.0087	–8.2		
1	Rh K	Rh–Rh (or –In)	1.5	0.268	0.0082	9.9	2.5	0.166–0.292
		Rh–Rh (or –In)	5.4	0.277	0.0070	5.5		
		Rh–Rh (or –In)	4.0	0.319	0.0090	9.8		
	In K	In–O	0.5	0.223	0.0076	9.9	0.7	0.126–0.279
		In–Rh (or –In)	5.5	0.277	0.0071	6.4		
		In–Rh (or –In)	4.1	0.320	0.0088	–4.0		
Rh foil	Rh K	Rh–Rh	12	0.268	0.0060	0	—	—
Rh ₂ O ₃	Rh K	Rh–O	6	0.206	0.0060	0	—	—

^a Coordination number. ^b Bond distance. ^c Debye–Waller factor. ^d Difference in the origin of photoelectron energy between the reference and the sample. ^e Residual factor.

and 0.32 nm shells, respectively). We did not use the calculation from the CN of the shell of fcc Rh phase because the small particle size of fcc Rh phase could decrease the CN, while tetragonal RhIn alloy particles were large enough. The calculated ratio was 36% and 68% for In/Rh = 0.5 and 1, respectively. The amount of tetragonal RhIn phase was also calculated by In XPS: the amount of In(0) corresponded to that of tetragonal RhIn; however the amount might be underestimated because not all atoms in larger RhIn alloy particles were detected by XPS analysis. The calculated values were 25% and 65% for In/Rh = 0.5 and 1, respectively, and in fact these values were smaller than those obtained from EXAFS.

Based on the above characterizations, we propose the model structure of Rh–In/C catalyst in this group ($0.2 < \text{In/Rh} \leq 1$) (Fig. 11). Small Rh metal particles (3 nm or less) partially covered with indium oxide species and large tetragonal RhIn alloy particles (~20 nm) are present on the support carbon. In addition, the large tetragonal RhIn particles are attached together, and dendritic structure is formed. The formation of large RhIn particles may be due to the low melting point of In(0). During the reduction process, In species that did not interact with Rh particle might be reduced to liquid In metal. The drops of liquid In metal moved on the support to collect many Rh particles, and large alloy particles were formed.

From the catalysis data (Fig. 1), the catalytic activity (TOF value) was sharply increased with the formation of tetragonal

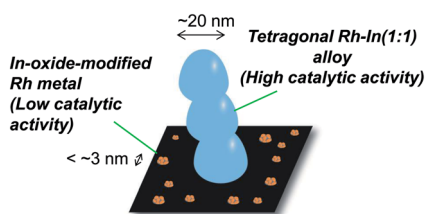


Fig. 11 Structure model of Rh–In/C (Rh 20 wt%, In/Rh = 0.5, 1).

RhIn phase. Therefore, we conclude that the catalytic activity of the different phases is in the following order: tetragonal RhIn alloy > Rh metal modified with indium oxide \gg unmodified Rh metal.

3.6. Characterization of Rh–In/C (Rh 20 wt%, In/Rh > 1) (group (iii))

The main phase in this group of catalyst was cubic RhIn. The width of the XRD peaks in the catalyst with In/Rh = 2 corresponded to the particle size of 20 nm. The TEM image of Rh–In/C (Rh 20 wt%, In/Rh = 2) is shown in Fig. 12a. There were spherical particles with various sizes from 10 nm to 100 nm. The EDX analysis of the particles (Fig. 12b) confirmed that the particles had the compositions of Rh : In = 1 : 1. As shown in Section 3.1, the In/Rh ratio in the net sample was 1.6. Therefore In species or In-rich domains were present in the sample, probably on carbon support. It should be noted that the CO adsorption amount of Rh–In/C (Rh 20 wt%, In/Rh = 2) was very low (CO/Rh = 0.006; Fig. 1). The cubic RhIn particles might be covered with In species.

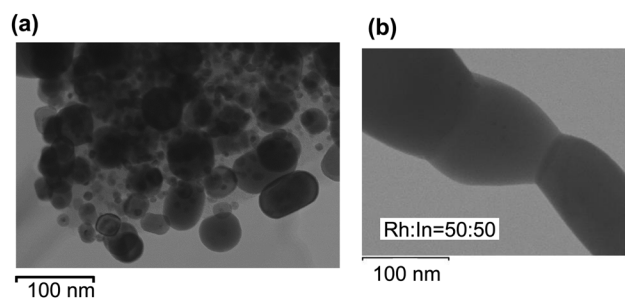


Fig. 12 TEM-EDX result of Rh–In/C (Rh 20 wt%, In/Rh = 2). (a) TEM image of particles on the support. (b) TEM image of the dendritic structure and the EDX analysis with Cliff–Lorimer method for the whole area.

3.7. Mechanism of activity promotion by In addition

Now we comment the nature of the activity of Rh–In bimetallic catalysts. It has been accepted that metal-catalyzed amination of alcohols proceeds *via* three steps: dehydrogenation of substrate alcohol to carbonyl compound ($R_1R_2CHOH \rightarrow R_1R_2C=O + H_2$), reaction of carbonyl compounds with ammonia to imines and water ($R_1R_2C=O + NH_3 \rightarrow R_1R_2C=NH + H_2O$), and hydrogenation of imine to amine product ($R_1R_2C=NH + H_2 \rightarrow R_1R_2CHNH_2$).⁶ In the previous paper, we showed that the rate-determining step of Rh–In/C-catalyzed amination is the dehydrogenation step based on the data of amination of optically pure substrate: rapid dehydrogenation before rate-determining step would induce racemization of substrate *via* dehydrogenation–hydrogenation, but in fact racemization of substrate was not observed at all.⁴ We also showed that the addition of In to Rh increases the resistance to the inhibition effect of amine/ammonia in the dehydrogenation step: while Rh metal has some activity in dehydrogenation of alcohols, the activity was almost totally suppressed by the presence of amines when indium was not added.⁴ It should be noted that the dehydrogenation activity of Rh–In/C was also higher than that of Rh/C even in the absence of amine/ammonia: the yield of hydroxyacetone, which is the dehydrogenation product from 1,2-propanediol, over Rh–In/C (5 wt% Rh, In/Rh = 1) was 3.1 times higher than that over Rh/C (5 wt% Rh).⁴ The difference of activity was even larger when the number of surface Rh atoms was taken into consideration. One explanation of activity increase by the presence of In is that the adsorption of amine, ammonia or carbonyl compound on surface Rh atom is weakened by the presence of In. The direct In–Rh bond is present in the two catalytically active structures (Rh metal particles partially covered with indium oxide and tetragonal RhIn alloy), and the number of Rh–In bond per Rh atom is larger in the more active phase (tetragonal RhIn alloy). The electronic effect of In addition to Rh center might induce the activity. The peak-top positions of XPS signal are listed in Table 5. The positions of Rh peaks were gradually shifted to lower binding energy by addition of In, and large shift was observed when alloy phase became dominant (In/Rh = 0.5 \rightarrow 1). It is difficult to conduct as detailed analysis of Rh bands as In (Fig. 4 and 7) because of the overlap of these Rh bands and C 1s band (Fig. S6, ESI†). The change of electronic structure may be also detected by XANES. From the Rh K-edge XANES data (Fig. S7, ESI†), addition of In up to In/Rh \geq 1 led a slight shift of the absolute edge position to

lower energy and slight decrease of white line intensity. The changes agreed with the shifts in XPS signal.

The low activity of In/Rh = 2 catalyst (cubic RhIn alloy) is not explained by this electronic effect. Cubic RhIn alloy was formed only when excess amount of In was present, and in fact the CO adsorption amount on Rh–In/C (20 wt% Rh, In/Rh = 2) was very low. Therefore, a number of In atoms were present on the cubic RhIn alloy surface. The surface In species might block the access of substrate molecule that is much larger than CO on the surface Rh atom.

We also mention the leaching of Rh and In during the reaction. As reported in the previous paper,⁴ leaching of both Rh and In from Rh–In/C (In/Rh = 1) was observed during the amination reaction, especially when carbon black support was used instead of activated carbon. In fact, the leaching accompanied the change of reaction medium into turbid colloidal solution even after the filtration. Increasing the loading amount from 5 wt% Rh to 20 wt%, the solution after reaction became much more turbid: the leaching problem was more evident. Based on the results in Section 3.5, especially TEM result, a part of Rh–In alloy phase might well be detached from the support and might become colloid. In other words, the cause of leaching can be the formation of Rh–In alloy colloid. The observed leaching of Rh, which as metallic state is insoluble in water, also supports this idea.

4. Conclusions

The structure of Rh–In/C with 20 wt% Rh changes with increasing In amount. At low In/Rh ratio (≤ 0.2), there are fcc Rh metal particles with ≤ 3 nm size on the carbon support, and the particles were partially covered with indium oxide species. Almost all In species were located on the Rh metal surface. More addition of In leads to the transformation of Rh particles to tetragonal RhIn alloy. The tetragonal RhIn alloy, which has not been reported in the literature, is the distorted structure ($a = 0.315$ nm and $c = 0.328$ nm) of cubic RhIn phase with CsCl structure ($a = 0.320$ nm). The tetragonal RhIn alloy forms large particles (~ 20 nm), and the particles are attached together to form dendritic solid. The transformation lasts until In/Rh = 1, at which the catalyst shows the highest turnover frequency for amination of alcohols. Above In/Rh = 1, the structure further changes into cubic RhIn alloy covered with indium species. The catalytic activity of phases is decreased in the following order: tetragonal RhIn alloy > Rh particles partially covered with In > Rh particles without In ~ 0 .

Acknowledgements

This work was supported by the Cabinet Office, Government of Japan through its “Funding Program for Next Generation World-Leading Researchers”.

References

- 1 V. Ponec, *Appl. Catal., A*, 2001, **222**, 31–45.
- 2 A. K. Singh and Q. Xu, *ChemCatChem*, 2012, **5**, 652–676.

Table 5 XPS peak-top positions of Rh–In/C (Rh 20 wt%)

In/Rh	Binding energy/eV	
	Rh 3d _{5/2}	Rh 3d _{3/2}
0.1	307.40	312.15
0.2	307.35	312.10
0.5	307.32	312.03
1	306.81	311.44
2	306.69	311.31

- 3 J. Shi, *Chem. Rev.*, 2013, **113**, 2139–2181.
- 4 T. Takanashi, Y. Nakagawa and K. Tomishige, *Chem. Lett.*, 2014, **43**, 822–824.
- 5 K. S. Hayes, *Appl. Catal., A*, 2001, **221**, 187–195.
- 6 S. Bähn, S. Imm, L. Neubert, M. Zhang, H. Neumann and M. Beller, *ChemCatChem*, 2011, **3**, 1853–1864.
- 7 M. Pera-Titus and F. Shi, *ChemSusChem*, 2014, **7**, 720–722.
- 8 P. Reyes, M. C. Aguirre, J. L. G. Fierro, G. Santori and O. Ferretti, *J. Mol. Catal. A: Chem.*, 2002, **184**, 431–441.
- 9 S. Koso, N. Ueda, Y. Shinmi, K. Okumura, T. Kizuka and K. Tomishige, *J. Catal.*, 2009, **267**, 89–92.
- 10 S. Koso, I. Furikado, A. Shimao, T. Miyazawa, K. Kunimori and K. Tomishige, *Chem. Commun.*, 2009, 2035–2037.
- 11 T. Miyake, T. Makino, S. Taniguchi, H. Watanuki, T. Niki, S. Shimizu, Y. Kojima and M. Sano, *Appl. Catal., A*, 2009, **364**, 108–112.
- 12 G. Beamson, A. J. Papworth, C. Philipps, A. M. Smith and R. Whyman, *J. Catal.*, 2010, **269**, 93–102.
- 13 G. Beamson, A. J. Papworth, C. Philipps, A. M. Smith and R. Whyman, *J. Catal.*, 2011, **278**, 228–238.
- 14 M. Chia, B. J. O'Neill, R. Alamillo, P. J. Dietrich, F. H. Ribeiro, J. T. Miller and J. A. Dumesic, *J. Catal.*, 2013, **308**, 226–236.
- 15 T. Buntara, I. Melián-Cabrera, Q. Tan, J. L. G. Fierro, M. Neurock, J. G. de Vries and H. J. Heeres, *Catal. Today*, 2013, **210**, 106–116.
- 16 S. Furukawa, Y. Yoshida and T. Komatsu, *ACS Catal.*, 2014, **4**, 1441–1450.
- 17 Y. Nakagawa, M. Tamura and K. Tomishige, *J. Mater. Chem. A*, 2014, **2**, 6688–6702.
- 18 U. Prüsse, M. Hähnlein, J. Daum and K.-D. Vorlop, *Catal. Today*, 2000, **55**, 79–90.
- 19 F. A. Marchesini, S. Irusta, C. Querini and E. Miró, *Appl. Catal., A*, 2008, **348**, 60–70.
- 20 F. B. Passos, D. A. G. Aranda and M. Schmal, *J. Catal.*, 1998, **178**, 478–488.
- 21 P. Ciavarella, D. Casanave, H. Moueddeb, S. Miachon, K. Fiaty and J.-A. Dalmon, *Catal. Today*, 2001, **67**, 177–184.
- 22 F. A. Marchesini, S. Irusta, C. Querini and E. Miró, *Catal. Commun.*, 2008, **9**, 1021–1026.
- 23 P. Sun, G. Siddiqi, W. C. Vining, M. Chi and A. T. Bell, *J. Catal.*, 2011, **282**, 165–174.
- 24 G. Onyestyák, *Catal. Commun.*, 2013, **38**, 50–53.
- 25 B. H. Verbeek, H. W. A. M. Rompa, P. K. Larsen, M. S. Methfessel and F. M. Mueller, *Phys. Rev. B: Condens. Matter Mater. Phys.*, 1983, **28**, 6774–6779.
- 26 P. Anres, P. Fossati, M. Gaune-Escard and J. P. Bros, *J. Alloys Compd.*, 1998, **266**, 241–246.
- 27 H. Okamoto, *Bull. Alloy Phase Diagrams*, 1988, **9**, 703.
- 28 D. Swenson, Sutopo and Y. A. Chang, *J. Alloys Compd.*, 1994, **216**, 67–73.
- 29 K. Kunimori, Y. Uchijima, M. Yamada, H. Matsumoto, T. Hattori and Y. Murakami, *Appl. Catal.*, 1982, **4**, 67–81.
- 30 <http://www.rsc.org/periodic-table/element/49/indium>.
- 31 K. Tomishige, K. Asakura and Y. Iwasawa, *J. Catal.*, 1994, **149**, 70–80.
- 32 Y. Amada, Y. Shinmi, S. Koso, T. Kubota, Y. Nakagawa and K. Tomishige, *Appl. Catal., B*, 2011, **105**, 117–127.
- 33 T. Ebashi, Y. Ishida, Y. Nakagawa, S. Ito, T. Kubota and K. Tomishige, *J. Phys. Chem. C*, 2010, **114**, 6518–6526.
- 34 J. Moulder, W. Stickle, P. Sobol and K. Bomben, *Handbook of X-ray Photoelectron Spectroscopy*, Physical Electronics Inc., Chanhassen, 1995.
- 35 E. van Cappellen, *Microsc., Microanal., Microstruct.*, 1990, **1**, 1–22.